From cell intercalation to flow, the importance of T1 transitions

Harish P. Jain [1,*] Axel Voigt,[2,3,4] and Luiza Angheluta [1]
[1]*Njord Centre, Physics Department, University of Oslo, Oslo, Norway*
[2]*Institute of Scientific Computing, TU Dresden, 01069 Dresden, Germany*
[3]*Center for Systems Biology Dresden, Pfotenhauerstr. 108, 01307 Dresden, Germany*
[4]*Cluster of Excellence, Physics of Life, TU Dresden, Arnoldstr. 18, 01307 Dresden, Germany*

(Received 28 March 2024; accepted 15 July 2024; published 15 August 2024)

T1 transitions, also called cell intercalations, are important sources of fluidization of epithelial cell monolayers. We use a multiphase field model to quantify this tissue fluidization in terms of the relative dispersion of cells and characterize the T1 flow profile. We show that the ensemble-averaged flow profile of a T1 transition has a saddle-point pattern accompanied by a localized burst in cell speed. Although the temporal evolution of the relative dispersion of cells depends on specific model details, the different dispersion curves collapse robustly onto a linear function of the number of T1 transitions, implying an important connection between T1 transitions and mixing in dense systems.

DOI: 10.1103/PhysRevResearch.6.033176

I. INTRODUCTION

Spontaneous flows within epithelial monolayers play a pivotal role in many biological processes including tissue development, wound healing, angiogenesis, and invasion of cancer cells [1–3]. In confluency, cells may migrate collectively while maintaining contact with their neighboring cells, thus preserving cell-cell junctions [1]. However, cells may also migrate relative to each other through structural rearrangements mediated by local events of remodeling of cell-cell junctions. Three main types of cell rearrangements have been distinguished [4–6]. A T1 transition is an event whereby two neighboring cells move apart while two of their neighbors move toward each other and make contact. This corresponds to an event where one junction disappears while another nucleates at the same site and orthogonal to the initial junction. A T2 transition occurs during extrusion/apoptosis events where cells are eliminated from the monolayer corresponding to vanishing junctions. By contrast, a T3 transition is an event associated with cell division inducing the nucleation of new junctions. Notably, T1 events preserve the total cell count within the monolayer, distinguishing them from T2 and T3 transitions.

T1 transitions have been observed in both epithelial [7] and mesenchymal [8] tissues and are important across different stages of gastrulation and organogenesis [9] as well as during cancer metastasis [10]. Empirical evidence shows that myosin II contributes to the buildup of tension at cell-cell junctions, thereby controlling T1 transitions in epithelial tissues [11,12]. However, the interplay between mechanical and biochemical signaling in these events remains a topic of debate [13]. There have been several studies aimed at characterizing the mechanical influence of T1 transitions in tissues [5,6,14–18] and in simulations [15,19–21].

Tissue flow has been explored mostly using coarse-grained approaches for active nematics, active polar matter, and more generally, for active p-atic liquid crystals, whereby spontaneous flows are influenced by their topological defects [22–24]. Several experimental studies have reported on different discrete orientational order (nematic, polar, or in general, p-atic) of cell tissues, corresponding to different lowest-energy topological defects [24–26]. This system dependency may be attributed to different types of cell lines but may also signal that the system is far from a hydrodynamic limit with a well-defined discrete symmetry, thus making the identification of relevant group symmetries and corresponding topological defects a matter of debate. On the other hand, it is becoming more evident that T1 transitions are important sources of tissue flow [19,27]. Qualitative differences between flows occurring at hydrodynamic scales and those induced by structural rearrangements of cells have been identified by comparing hydrodynamic (continuum) simulations with cell-resolved (discrete) simulations [23,28]. How the flows originating at the discrete cell level influence the tissue flow at hydrodynamic scales is far less explored and understood.

In this paper, we aim to bridge this gap to better understand the generic flow patterns due to cell neighbor rearrangements. Within a multiphase field model for a flat and confluent cell monolayer, as discussed in Sec. II, we can compute the average flow profile of a T1 transition, as presented in Sec. III. We demonstrate that T1 transitions are short-lived events of neighbor exchanges, where the involved cells acquire high-speeds and generate fourfold vorticity with alternating circulation. Within our setup, where the total number of cells and their size are fixed, and by using a Lagrangian approach, we demonstrate in Sec. IV that the cell pair dispersion is

*Contact author: harishpj@fys.uio.no

Published by the American Physical Society under the terms of the Creative Commons Attribution 4.0 International license. Further distribution of this work must maintain attribution to the author(s) and the published article's title, journal citation, and DOI.

mediated solely by T1 transitions. We predict a robust scaling of the mean pair separation with the number of T1 transitions, which hints at a generic mechanism of relative dispersion by structural rearrangements. Concluding remarks are presented in Sec. V.

II. MULTIPHASE FIELD MODEL

We model the confluent cell monolayer using the multiphase field modeling approach as in Refs. [29–34] and as discussed in a recent review [35]. Our specific model formulation follows Ref. [19] and is used to simulate the dynamics of a confluent monolayer of $N = 100$ cells. Each cell is described by a phase field variable ϕ_i, with $i = 1, 2, \ldots, N$, which has the bulk values $\phi_i \approx 1$ inside the cell, $\phi_i \approx -1$ outside it, and with a diffuse interface of width $O(\epsilon)$ between them representing the cell boundary. The phase field ϕ_i follows the conservative dynamics:

$$\partial_t \phi_i + \mathbf{v}_i \cdot \nabla \phi_i = \Delta \frac{\delta \mathcal{F}}{\delta \phi_i}, \tag{1}$$

which preserves the area of a cell (incompressible cells). The diffusive relaxation is controlled by minimization of the free energy functional $\mathcal{F} = \mathcal{F}_{\mathrm{CH}} + \mathcal{F}_{\mathrm{REP}} + \mathcal{F}_{\mathrm{ADH}}$. The free energy contains the Cahn-Hilliard energy in degenerate form [36]:

$$\mathcal{F}_{\mathrm{CH}} = \frac{1}{Ca} \sum_{i=1}^{N} \int_{\Omega} g(\phi_i) \left[\frac{\epsilon}{2} ||\nabla \phi_i||^2 + \frac{1}{4\epsilon} \left(\phi_i^2 - 1\right)^2 \right] d\mathbf{x}, \tag{2}$$

where ϵ controls the interface width, Ca is a parameter for tuning the cell deformability, and

$$g(\phi_i) = \frac{2}{3\sqrt{(\phi_i + 1)^2 (\phi_i - 1)^2}}$$

is a term to prevent bulk diffusion ensuring $\phi_i \in [-1, 1]$, without affecting the asymptotic behavior as $\epsilon \to 0$ [36]. In addition, there are two interaction energies, where

$$\mathcal{F}_{\mathrm{REP}} = \frac{a_r}{2In} \sum_{i=1}^{N} \int_{\Omega} \sum_{j \neq i} (\phi_i + 1)^2 (\phi_j + 1)^2 d\mathbf{x} \tag{3}$$

is the repulsion energy to prevent overlap of cell interior, and

$$\mathcal{F}_{\mathrm{ADH}} = \frac{a_a}{2In} \sum_{i=1}^{N} \int_{\Omega} \sum_{j \neq i} \left(\phi_i^2 - 1\right)^2 \left(\phi_j^2 - 1\right)^2 d\mathbf{x} \tag{4}$$

is the adhesion energy that promotes overlap of cell boundaries. In denotes the interaction strength, and a_r and a_a are parameters to tune contribution of repulsion and adhesion energy, respectively. The adhesive part differs from Ref. [19] by rewriting the interaction using the equilibrium condition $\frac{\epsilon}{2} \|\nabla \phi_i\|^2 \approx \frac{1}{4\epsilon} (\phi_i^2 - 1)^2$, see Refs. [33,37–40].

Cell activity is introduced as self-propulsion of each cell through the advection term. The cell advection field is given as

$$\mathbf{v}_i(\mathbf{x}, t) = v_0 \mathbf{e}_i(t) \hat{\phi}_i(\mathbf{x}, t), \tag{5}$$

where v_0 is used to tune the magnitude of activity:

$$\hat{\phi}_i = \frac{\phi_i + 1}{2}, \tag{6}$$

TABLE I. Default values of the model parameters. dt denotes the time step size.

L	T	ϵ	v_0	Ca	In	a_a	a_r	D_r	α	r_{active}	dt
100	150	0.15	0.5	0.2	0.1	1	1	0.01	0.1	1	0.005

and $\mathbf{e}_i = [\cos\theta_i(t), \sin\theta_i(t)]$ is the direction of self-propulsion. The migration orientation $\theta_i(t)$ evolves diffusively with a drift that aligns with the principal axis of cell elongation as

$$d\theta_i = \sqrt{2D_r} dW_i(t) + \alpha[\beta_i(t) - \theta_i(t)]dt, \tag{7}$$

where D_r is the rotational diffusivity, and W_i is the Wiener process.

The cell elongation is identified by the principal eigenvector $\boldsymbol{\eta}_i^+$ of the shape deformation tensor, as described in Ref. [34]. Here, $\beta_i(t)$ is the orientation of the cell elongation and defined as

$$\beta_i(t) = \begin{cases} \arg[\boldsymbol{\eta}_i^+(t)] : \mathbf{e}_i(t) \cdot \eta_i^+(t) > 0 \\ -\arg[\boldsymbol{\eta}_i^+(t)] : \mathbf{e}_i(t) \cdot \eta_i^+(t) < 0. \end{cases} \tag{8}$$

The parameter α controls the time scale of this alignment. Setting $v_0 = 0$ for some cells allows for the modeling of a mixture of active self-propelled cells and passive cells. The activity ratio r_{active} is the fraction of cells for which $v_0 > 0$.

Equation (1) is solved numerically on a square domain $\Omega = [0, L] \times [0, L]$ (where $L = 100$) using periodic boundary conditions for the time $[0, T]$. We are using the finite element method within the toolbox AMDiS [41,42] and the parallelization concept introduced in Ref. [43], which considers each cell on a different core and accounts for short-range interaction between cells to reduce the communication. The system of partial differential equations is discretized in time using a semi-implicit approach. Time step size and mesh resolution are related to ensure stability. For further details and numerical tests, see earlier work from Refs. [19,35,38].

The values of the model parameters are listed in Table I, unless specified otherwise. Movie 1 in the Supplemental Material (SM) [44] shows the cell boundaries in a simulation as per parameters in Table I.

III. FLOW PROFILE OF T1 TRANSITIONS

A T1 transition reconfigures the junctions between neighboring cells as illustrated in Figs. 1(a)–1(c). The two three-way vertices represented by red dots move toward each other, shrinking the corresponding junction [Fig. 1(a)]. Within multiphase field models, T1 transitions occur spontaneously as cells deform and move as a result of activity. Further, in multiphase field models, a T1 transition has a finite duration [19] that starts when the junction vanishes, creating a transient extracellular gap (approximated as a four-way vertex), as shown in Fig. 1(b). The T1 transition concludes when a new pair of three-way vertices nucleate, forming a new junction, as in Fig. 1(c). We define the orientation ζ of a T1 transition as the angle of the newly formed junction with respect to the x axis. We use this angle ζ to reorient different T1

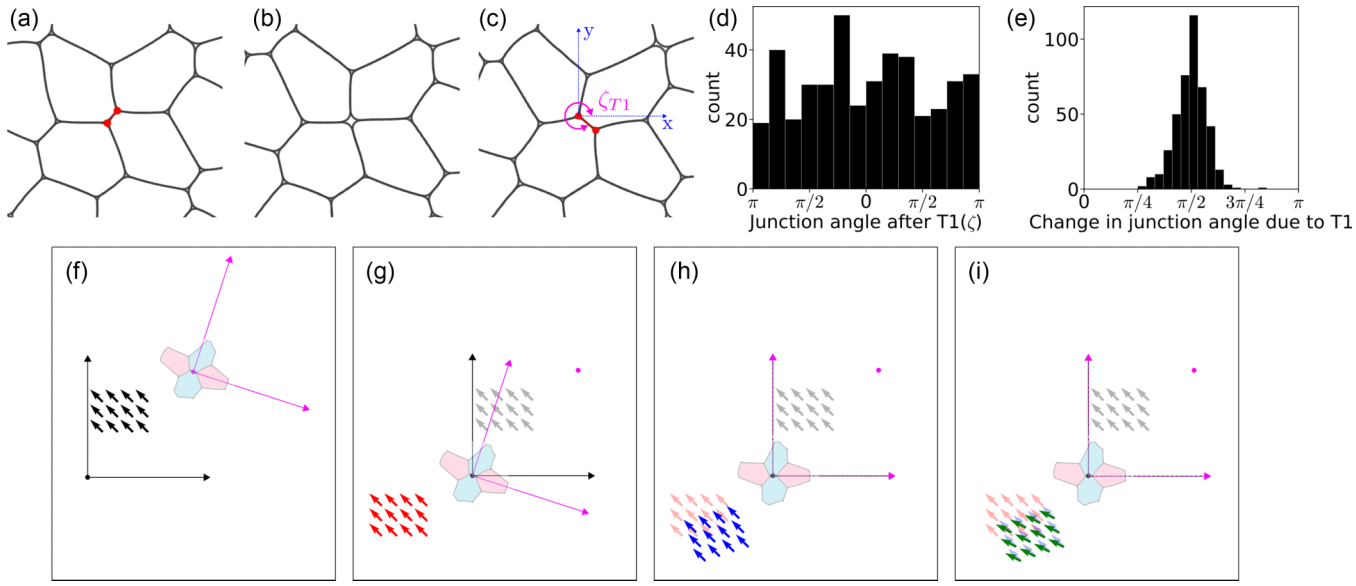

FIG. 1. Configuration of four cells (a) before, (b) during, and (c) after a T1 transition. The three-way vertices involved in the T1 are marked by red dots. Junction angle ζ is the orientation of the newly formed junction after a T1 transition measured counterclockwise from the positive x semiaxis. (d) Histogram of the junction angle after a T1 transition ζ. (e) Histogram of change in junction angle due to the T1 transition. Steps involved in transformation of the velocity field to align it with respect to a T1 transition: (f) A small section of a field is shown in black. A T1 transition is shown with the cells that lose neighbors colored in pink, while the cells that gain neighbors are colored in blue. A magenta reference frame is attached to the epicenter of the T1 and is aligned with the orientation of the T1, ζ. (g) The epicenter is shifted to the origin. (h) The frame is rotated to align with the horizontal axis. (i) The orientation of the vector field is rotated by ζ_{T1}.

transitions and their velocity profiles to compute ensemble-averaged transient flows, as described next.

A. Ensemble average

We start by computing the T1 orientation angle ζ_m of the mth T1 transition in an ensemble of N_{T1} T1 events.

Let us denote the four cells associated with one T1 transition by $A, B, C,$ and D. Before a T1, let the list of cell neighbor pairs be

$$\text{Before T1: } (A, B), (A, C), (A, D), (C, B), (D, B).$$

Suppose, at the start of a T1 transition, cells A and B lose contact, and at the end of the T1 transition, cells C and D make contact. This changes the cell neighbor list to

$$\text{After T1: } (C, D), (A, C), (A, D), (C, B), (D, B).$$

We denote the start and end times of the mth T1 transition as $t_{m,s}$ and $t_{m,e}$, respectively. Before $t_{m,s}$, the three-way vertices where the cells (A, B, C) and (A, B, D) meet move toward each other, shrinking the common junction between them, and eventually, the junction vanishes at $t_{m,s}$. Between $t_{m,s}$ and $t_{m,e}$, there is an extracellular gap between the four cells. After $t_{m,e}$, two new three-way vertices where the cells (A, C, D) and (B, C, D) meet are created, and they move away from each other. Let $\mathbf{s}_{m,1}$ and $\mathbf{s}_{m,2}$ be the positions of the two three-way vertices a short time after $t_{m,e}$. The orientation of the new junction between $\mathbf{s}_{m,1}$ and $\mathbf{s}_{m,2}$ is $\zeta_m = \arg(\mathbf{s}_{m,1} - \mathbf{s}_{m,2})$. This is also illustrated in Fig. 1(c). Similarly, we can also compute the orientation of the old junction before the mth T1 transition. Figure 1(d) shows the histogram of the orientations of N_{T1} T1 transitions, which implies that the orientations of the T1 transitions are close to being uniformly distributed. Figure 1(e) shows the histogram of the difference in junction angle before and after the T1 transition. The histogram peaks at around $\pi/2$, implying that the junctions before and after a T1 transition are mostly perpendicular to each other.

For each T1 transition, we also find the location of its epicenter as we have done in Ref. [19]. The epicenter is defined as the location of a point whose sum of distances to the four cells involved in the T1 transition is the minimum, at the midpoint time $\frac{t_{m,s}+t_{m,e}}{2}$. We denote the location of the epicenter of the mth T1 transition by $\mathbf{s}_{m,c}$. Essentially, this point lies within the gap formed between the four cells during the T1 transition.

At any given time t, we define the global velocity field as

$$\mathbf{v}_g(\mathbf{x}, t) = \sum_{i=1}^{N} \hat{\phi}_i(\mathbf{x}, t) \frac{\mathbf{r}_i(t) - \mathbf{r}_i(t - dt)}{dt}, \tag{9}$$

where $\mathbf{r}_i(t)$ is the location of the center of the ith cell at time t, and dt is the time step size. Therefore, $\mathbf{v}_g(\mathbf{x}, t)$ in the interior of a cell is equal to the velocity of the center of mass of the cell.

For the mth T1 transition, at any time t, we can transform the global field to obtain its *T1 flow velocity field* as

$$\mathbf{v}_m(\mathbf{x}, t) = \mathbf{R}_{\zeta_m} \mathbf{v}_g[\mathbf{R}_{\zeta_m}(\mathbf{x} - \mathbf{s}_{m,c}), t], \tag{10}$$

where $\mathbf{R}_{\zeta_m}$ is the two-dimensional (2D) rotation matrix with rotation angle ζ_m. This $\mathbf{v}_m(\mathbf{x}, t)$ is centered such that the epicenter is at the origin, and the junction formed after the T1 transition is aligned along the horizontal axis. Figures 1(f)–1(i) visualize the transformation from $\mathbf{v}_g(\mathbf{x}, t)$

to $\mathbf{v}_m(\mathbf{x}, t)$ in three steps for an arbitrary field: (i) the field is translated such that the origin coincides with the epicenter of the T1 transition; (ii) the grid is rotated such that the junction formed after the T1 transition aligns along the horizontal axis; and (iii) the vectors themselves are rotated while being fixed in space to reflect the right orientation with respect to the epicenter. Periodic boundary conditions are considered while transforming the fields by numerically wrapping the computational domain.

Let an arbitrary field f at time τ before and after a T1 transition be denoted by $f(\mathbf{x}, t_{m,s} - \tau)$ and $f(\mathbf{x}, t_{m,e} + \tau)$, respectively. We consider the ensemble average over the N_{T1} transitions measured at time relative to the start or end of a T1 transition as $\langle f(t_{m,e/s} \pm \tau)\rangle = \frac{1}{N_{T1}} \sum_{m=1}^{N_{T1}} f(t_{m,e/s} \pm \tau)$. With this, we define the average of the T1 flow velocity field at time τ after/before T1 as

$$\mathbf{v}_{T1}^{\pm}(\mathbf{x}, \tau) = \langle \mathbf{v}_m(\mathbf{x}, t_{m,e/s} \pm \tau)\rangle. \tag{11}$$

Similarly, the average magnitude of the T1 flow velocity field at τ is given as

$$\overline{v}_{T1}^{\pm}(\mathbf{x}, \tau) = \langle |\mathbf{v}_m(\mathbf{x}, t_{m,e/s} \pm \tau)|\rangle. \tag{12}$$

To further explore the directional motion, we define the average velocity polarization field as

$$\mathbf{p}_{T1}^{\pm}(\mathbf{x}, \tau) = \left\langle \frac{\mathbf{v}_m(\mathbf{x}, t_{m,e/s} \pm \tau)}{|\mathbf{v}_m(\mathbf{x}, t_{m,e/s} \pm \tau)|} \right\rangle, \tag{13}$$

such that $|\mathbf{p}_{T1}^{\pm}| \in [0, 1]$, where $|\mathbf{p}_{T1}^{\pm}| = 0$ corresponds to randomly oriented T1 flow velocities, and $|\mathbf{p}_{T1}^{\pm}| = 1$ for preferred directional orientation of T1 flow velocities.

In Figs. 2(a) and 2(c) and Figs. 2(b) and 2(d), we plot $\mathbf{v}_{T1}^{-}(\mathbf{x}, 0)$ and $\mathbf{v}_{T1}^{+}(\mathbf{x}, 0)$, respectively. The streamlines suggest that the flow comprises quadrupolar vortices with alternating circulation centered at the epicenter. The flow has a saddle-point structure, allowing us to identify the vertical axis of cells making contact and horizontal axis of cells breaking contact. The time evolution of $\mathbf{v}_{T1}^{-}$ and $\mathbf{v}_{T1}^{+}$ is shown in Movies 2 and 3, respectively in the SM [44]. The magnitudes in Figs. 2(a) and 2(b) correspond to $|\mathbf{p}_{T1}^{-}(\mathbf{x}, 0)|$ and $|\mathbf{p}_{T1}^{+}(\mathbf{x}, 0)|$. The approximate profile of the four cells involved in the T1 transition can be discerned by the high values of $|\mathbf{p}_{T1}|$ around the epicenter. The values of $|\mathbf{p}_{T1}|$ inform on the likelihood of the observed orientation of the streamlines, where a higher polarization indicates that the streamlines shown are more likely to occur. The low values of $|\mathbf{p}_{T1}|$ away from the epicenter suggest that cells that are not involved in a T1 do not have a preferred velocity orientation. The magnitudes in Figs. 2(c) and 2(d) correspond to $\overline{v}_{T1}^{-}$ and $\overline{v}_{T1}^{+}$. From Fig. 2(c), we discern that, at the end of a T1 transition, there is a localized surge of speed around the epicenter, suggesting cells involved in a T1 transition move faster than the rest of the cells in the monolayer. From Movie 5 in the SM [44], we see that the speed in the vicinity of the epicenter decays over time to the global average. Before a T1 transition, there is no such surge in $\overline{v}_{T1}$ observed near the epicenter (see Movie 4 in the SM [44]). These results are consistent with those in Ref. [19], where similar results were obtained for the evolution of average speed of the four cells involved in a T1 transition. It would be interesting to compare these flow profiles with the characteristic flow field of defects in coarse-grained active nematics, polar, or more generally, in active p-atic liquid crystals. The corresponding hydrodynamic models have been proposed in Refs. [45,46].

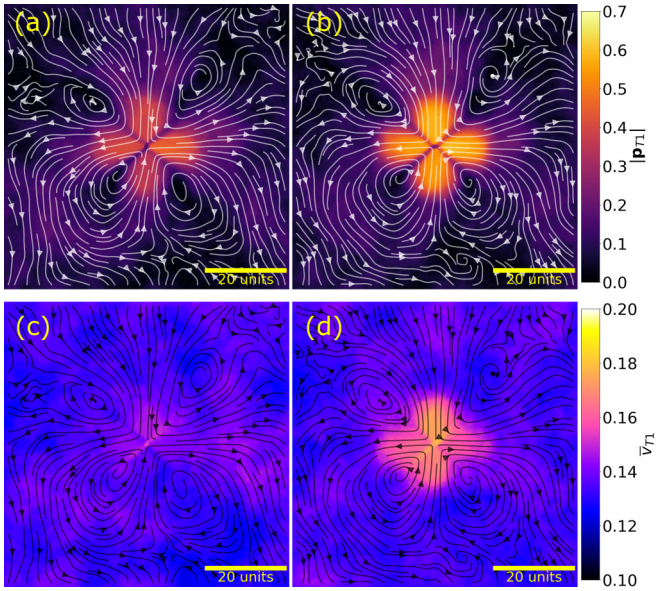

FIG. 2. Ensemble-averaged flow profile of T1 transitions. Streamlines in (a) and (c) correspond to flow at the start of a T1 transition $[\mathbf{v}_{T1}^{-}(\mathbf{x}, 0)]$, and those in (b) and (d) correspond to flow at the end of a T1 transition $[\mathbf{v}_{T1}^{+}(\mathbf{x}, 0)]$. Magnitude of the colormap in (a) and (b) correspond to $|\mathbf{p}_{T1}^{-}(\mathbf{x}, 0)|$ and $|\mathbf{p}_{T1}^{+}(\mathbf{x}, 0)|$. Magnitude of the colormap in (c) and (d) correspond to $\overline{v}_{T1}^{-}(\mathbf{x}, 0)$ and $\overline{v}_{T1}^{+}(\mathbf{x}, 0)$. The cell size (square root of cell area) is ∼10 units. The time evolution of these fields is shown in Movies 2–5 in the SM [44].

The source of this tissue flow is ultimately linked to the dispersion of cell motion. Cells that are caged among their neighbors undergo small shape fluctuations and experience resistance to their motion due to cell-cell interactions. However, these small fluctuations may build up and can bring two three-way vertices closer together. This leads to the accumulation of energy near those vertices. Eventually, this can induce a T1 transition releasing energy, thereby helping the cells to uncage. This is akin to the buildup prior to a slip event in stick-slip dynamics [47]. Provided there is no preferred orientation of the T1 transition [see Fig. 1(d)], the cells move away from their initial neighbors and disperse across the tissue. In the next section, we quantify the statistical properties of cell dispersion.

IV. CELL DISPERSION

The vortical flow induced by T1 transitions is reflected in the dispersion of cells relative to each other and thus in the mixing of cells. We can quantify the flow properties indirectly through the relative dispersion of cells. We use the center of mass denoted by $\mathbf{r}_i$ for the ith cell to track cell migration. The mean-squared displacement of the cells quantifies the single particle dispersion and is given as

$$\sigma^2(t) = \frac{1}{N} \sum_{i=1}^{N} |\mathbf{r}_i(t + t_0) - \mathbf{r}_i(t_0)|^2, \tag{14}$$

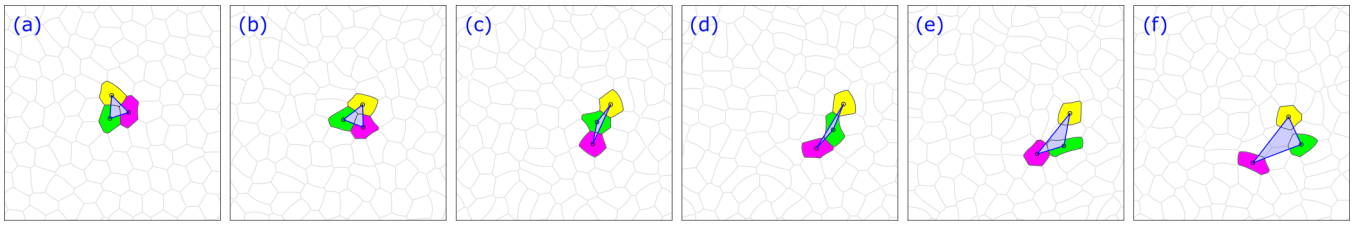

FIG. 3. Temporal snapshots of the evolution of a cell triplet. T1 transitions break the contact between cells in the triplet and increase the area spanned by the triplet.

where N is the total number of cells. This measures how far a cell has migrated from its initial location at t_0 in a time lag t. Similarly, the mean pair separation distance in a time lag t quantifies the relative dispersion and is defined as

$$\Pi(t) = \frac{1}{N_P(t_0)} \sum_{j=1}^{N_P(t_0)} |\mathbf{r}_{j,1}(t) - \mathbf{r}_{j,2}(t)|, \tag{15}$$

where $N_P(t_0)$ is the number of pairs of cells that were neighbors at an initial time t_0. Here, $\mathbf{r}_{j,1}$ and $\mathbf{r}_{j,2}$ are the positions of the two cells corresponding to the jth neighbor pair at t_0. To better quantify the dynamics of the three-way vertices, we also consider the dispersion of triplets. A triplet consists of three cells where each cell is a neighbor to the other two cells. Let $\mathbf{r}_{k,1}$, $\mathbf{r}_{k,2}$, and $\mathbf{r}_{k,3}$ be the positions of the three cells corresponding to the kth triplet. The corresponding lengths of the edges in the triplet triangle are $\bar{a} = |\mathbf{r}_{k,1} - \mathbf{r}_{k,2}|$, $\bar{b} = |\mathbf{r}_{k,2} - \mathbf{r}_{k,3}|$, and $\bar{c} = |\mathbf{r}_{k,3} - \mathbf{r}_{k,1}|$. Given the perimeter of the triangle $\bar{s} = \bar{a} + \bar{b} + \bar{c}$, the triangle area of the kth triplet is $A_k = \bar{s}(\bar{s} - \bar{a})(\bar{s} - \bar{b})(\bar{s} - \bar{c})$. Thus, we can also define the mean triplet separation area as

$$\Lambda(t) = \frac{1}{N_T(t_0)} \sum_{k=1}^{N_T(t_0)} A_k(t + t_0), \tag{16}$$

where $N_T(t_0)$ is the number of triplets of cells at time t_0. Here, $\Lambda(t)$ is the average area of all triangles made by a triplet of cells that were mutually adjacent at time t_0. Snapshots from the evolution of one such triplet triangle are shown in Fig. 3. Geometrically, the dispersion of cells is associated with deformations, translations, and rotations of the triplet triangle. See Appendix A for details on handling the periodic boundary conditions.

The initial area of the triplet triangles is nonzero and is related to the cell size. Notice that the cells remain mutually adjacent for a transient time until the three-way vertex shared between them is destroyed in a T1 transition by merging with another three-way vertex. From hereon, the cells are likely to further separate from each other due to subsequent T1 transitions. The triplet area can also collapse to zero when the three cells become collinear [see Figs. 3(c) and 3(d)].

Figures 4(a)–4(c) show the mean-squared displacement (σ^2) and relative dispersion of pairs (Π) and triplets (Λ) as

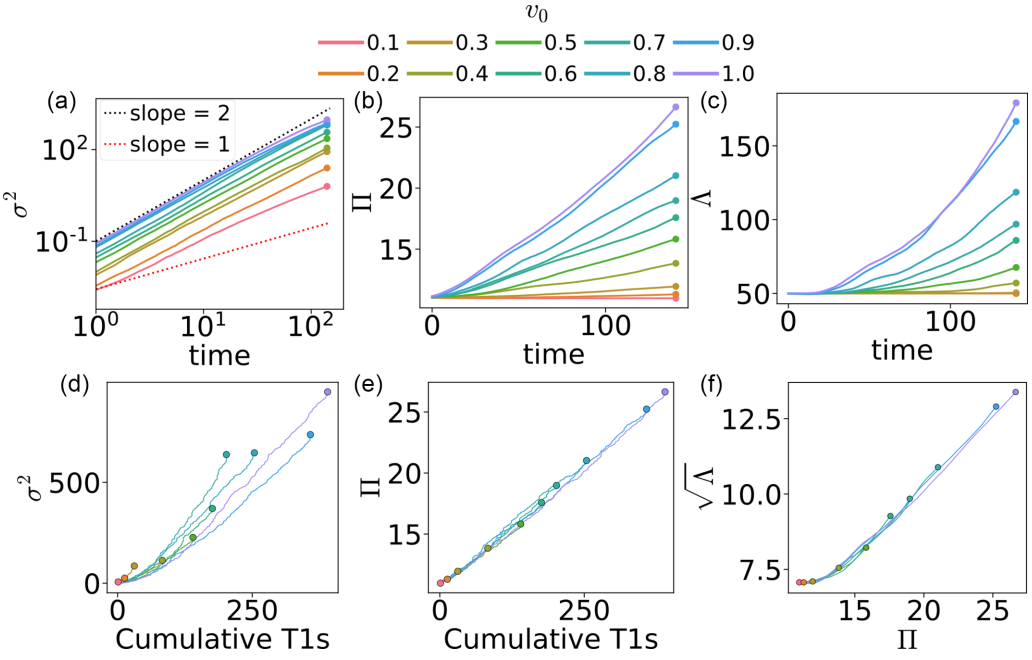

FIG. 4. Evolution of (a) σ^2, (b) Π, and (c) Λ plotted against time. (d) σ^2 and (e) Π plotted against the cumulative number of T1 transitions within the tissue. (f) $\sqrt{\Lambda}$ plotted against Π. Different colors correspond to different cell activities defined by the self-propulsion speed v_0 as per the legend at the top.

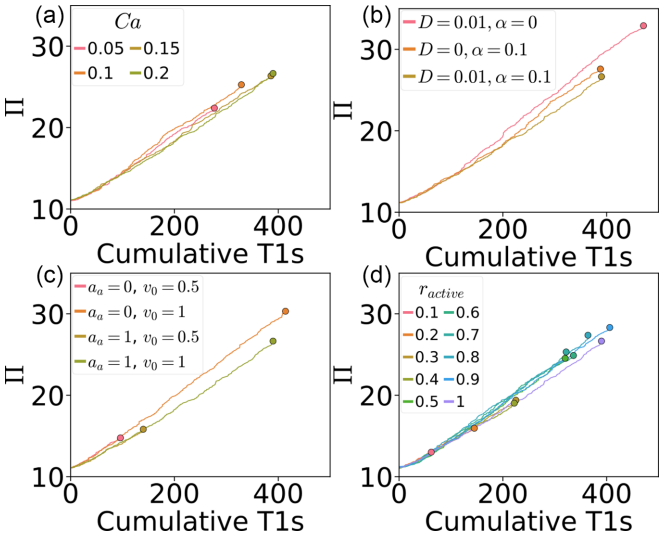

FIG. 5. Data collapse of the relative dispersion curves as a function of the cumulative T1 transitions for various model parameters and setups: (a) Cell deformability (Ca) is varied for $v_0 = 1$. (b) Rotational noise D and shape alignment α are varied for $v_0 = 1$. (c) Repulsion vs repulsion and adhesion cell-cell interaction. (d) Mixtures of active and passive cells with a fraction r_{active} of active cells with $v_0 = 1$.

functions of time lag t for different activities v_0. Within the computational time, we observe that the cells are superdiffusive with a scaling exponent that lies between 1 (normal diffusion limit) and 2 (ballistic limit). For all three quantities, their values at a given time lag increase with cell activity, which is consistent with the observation that the flow fluctuations increase with activity [22] (see also Appendix C). At low activities, we notice that there is almost no dispersion of cell pairs and triplets. While the pair separation Π increases with time lag, the triplet area $\Lambda(t)$ remains constant for a initial transient period. A single T1 transition would destroy the three-way vertex shared by the cells in the triplet, but two pairs out of three initial pairs in the triplet remain. The triplet area starts to diverge when at least one of the cells breaks contact with the other two cells in the triplet, which requires a minimum of two T1 transitions (see Appendix B). Thus, in this initial period, the area of the triplet triangle $A_k(t)$ fluctuates around $A_k(t_0)$. As the cells undergo further T1 transitions and move apart, the area spanned by the triplet Λ increases monotonically with the time lag.

Figures 4(d) and 4(e) show the net dispersion of single cells $[\sigma^2(t)]$ and cell pairs $[\Pi(t)]$ plotted against the cumulative number of T1 transitions within the tissue in time lag t. Interestingly, the curves for Π for different v_0 collapse into a linear master curve. A similar collapse is also present for the triplet area, which shows that these two quantities are directly related to the number of T1 transitions. However, this is not the case for σ^2 because cells can also migrate in local flocks, which affects σ^2 but does not change Π and Λ since the cell-cell connectivity is preserved [1]. In the absence of T1 transitions, cells are topologically caged within their neighbors, and this makes it difficult to generate flow fluctuations (when T2 and T3 transitions are also absent). It takes ∼250 T1 transitions across the tissue of 100 cells, or equivalently 10 T1 transitions per cell, for the mean pair separation to double its value. Two neighboring cells must undergo ∼10 T1 transitions each, such that their cell centers can be two cell widths apart. When $\sqrt{\Lambda}$ is plotted against Π, initially, $\sqrt{\Lambda}$ is constant, and later, it varies linearly with Π [see Fig. 4(f)].

To further explore the robustness of this data collapse, we also vary other model parameters, i.e., cell deformability Ca, rotational noise D, shape alignment α, adhesion parameter a_a, and activity ratio r_{active}. For high values of Ca, the cells are more deformable. The rotational diffusion coefficient D and the rate α at which cells tend to align their preferred direction of motion with the direction of their elongation control the dynamics of the self-propulsion mechanism. For $a_a = 0$, the interactions between cells are purely repulsive, while $a_a > 0$ corresponds to additional attractive interaction between cells. Here, r_{active} is the fraction of cells which have nonzero activity. The mean pair separation distance as a function of cumulative number of T1 transitions for these scenarios is plotted in Fig. 5. In all these scenarios, we see similar scaling behavior, suggesting that T1 transitions affect relative dispersion in similar ways irrespective of model parameters.

V. DISCUSSION AND CONCLUSIONS

In summary, we have put forward a quantitative way to study the connection between T1 transitions, tissue fluidization, and cell dispersion. We have shown that T1 transitions, as topological events of neighbor exchanges, are transient and localized saddle-point flows generating fourfold vortices. The average polarization is high and localized along the principal axes of the saddle point centered at the epicenter of a T1 transition, showing that there is persistent directional flow along these directions which feeds to vortical flow over longer distances. Such flows could possibly contribute to active turbulence within the monolayer [22].

We have demonstrated that tissue flows where cells disperse relative to each other are promoted solely by T1 transitions. While the temporal behavior of the cell dispersion (single, pair, or triplet) depends on the model parameters, we found a robust linear dependence of the relative dispersion of pairs and triplets of cells on the number of T1 transitions. The data collapse of the different dispersion curves onto a linear master curve suggests that the rate of relative dispersion is directly proportional to the occurrence rate of T1 transitions regardless of the underlying nucleation mechanism. This unveils a deeper connection between topological rearrangements and mixing in densely packed systems, in general. As relative dispersion and the number of T1 transitions are measurable observables also in experimental studies of epithelial cell monolayers, our model predictions are accessible for future experimental validation.

ACKNOWLEDGMENTS

L.A. and H.P.J. acknowledge funding by the European Union's Horizon 2020 research and innovation programme under the Marie Skłodowska-Curie Grant Agreement No. 945371. A.V. acknowledges funding by the German Research Foundation within Grant No. FOR3013. We are grateful for

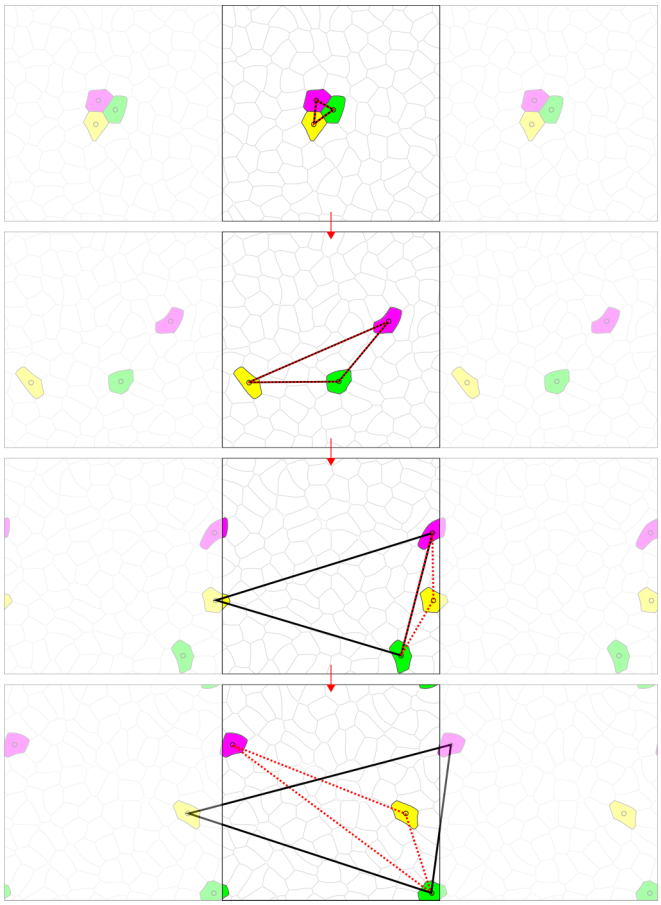

FIG. 6. The triangle with red-dotted sides is connected to the cells in the computational domain, while the triangle with black sides is connected to the location of the cells in an infinite two-dimensional (2D) domain. Time evolves from top to bottom.

discussions with Amin Doostmohammadi, Richard D. J. G. Ho, Per Arne Rikvold, and Dag K. Dysthe.

APPENDIX A: PERIODIC BOUNDARY CONDITIONS

While the general notion of periodic boundary conditions is standard, the definition of the mean dispersion of a single cell (σ^2), cell pairs (Π), and triplets (Λ) requires some additional thought. We essentially assume that, when a cell crosses the periodic boundary, it moves into an identical but distinct copy of the domain that lies adjacent to the domain, as illustrated in Fig. 6. The history of the cell motion is used to determine the modified location of center of mass in the resulting infinite domain.

APPENDIX B: TRIAD DISPERSION

Figure 7 shows an illustration of a section of a hexagonal lattice comprising hexagonal cells. A triangle is marked that joins the cell centers of the three red cells. In the left figure, all three cells are mutually adjacent, while on the right figure, two of the three cells are not in contact. The areas of the triangles are the same in both situations. For a triplet area to diverge significantly, at least one of the three cells must break contact

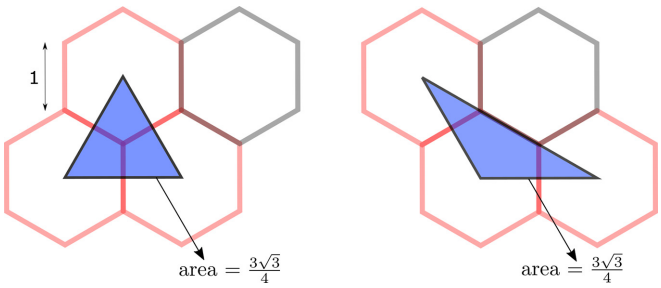

FIG. 7. A triangle joining 3 red cells is shown when (left) all 3 cells are mutually adjacent and (right) one pair are not neighbors.

from the other two cells. This is why, multiple T1 transitions per triplet are required before the mean triplet separation area (λ) starts to increase significantly.

APPENDIX C: GLOBAL STATISTICS

Figures 8(a) and 8(b) show the single-particle dispersion $[\sigma(T)]$ and relative dispersion $[\Pi(T)]$ at a given time lag T as a function of cell activity v_0 and deformability Ca. Both quantities increase monotonically with v_0; only the relative dispersion is sensitive to Ca. This suggests that, on average, cells tend to spread out at the same rate regardless of whether they are stiffer or softer. Nonetheless, stiffer cells tend to disperse less relative to each other than softer cells. To quantify, the collective flocking motion of the cells, we compute the global polar order at a given time as

$$\psi(t) = \frac{1}{N}\left|\sum_{i=1}^{N}\frac{[\mathbf{r}_i(t) - \mathbf{r}_i(t')]}{t - t'}\right|, \tag{C1}$$

such that $\psi(t) \approx 1$ corresponds to cells moving as a flock in the same direction, while $\psi(t) \approx 0$ represents cells moving uncoordinatedly and in random directions. In Fig. 8(c), we see the flocking tendency is higher for stiffer cells. This is

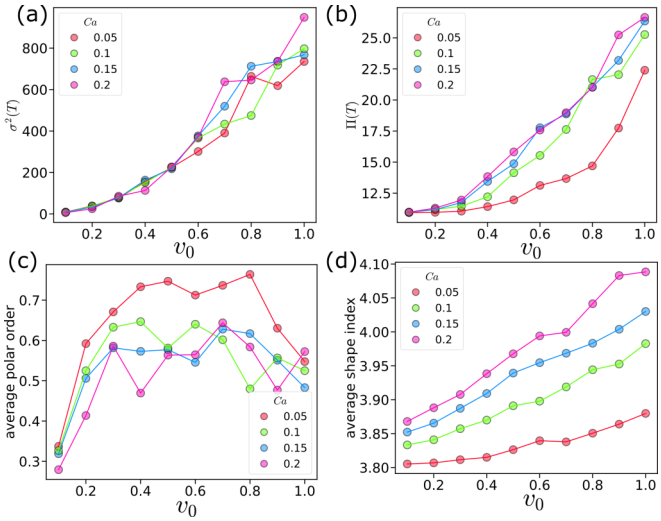

FIG. 8. (a) Mean-squared displacement and (b) mean pair separation for the time lag $T = 150$. (c) Average polar order. (d) Average shape index.

consistent with their tendency to preserve their neighbors (disperse less relative to each other) that helps coordinate their motion better. In Fig. 8(d), we see that the average cell shape index, defined by the ratio of the perimeter of cells to the square root of area of the cells, also increases monotonically with activity and cell deformability.

[1] B. Ladoux and R. M. Mège, Mechanobiology of collective cell behaviours, Nat. Rev. Mol. Cell Biol. **18**, 743 (2017).

[2] A. Brugués, E. Anon, V. Conte, J. H. Veldhuis, M. Gupta, J. Colombelli, J. J. Muñoz, G. W. Brodland, B. Ladoux, and X. Trepat, Forces driving epithelial wound healing, Nat. Phys. **10**, 683 (2014).

[3] P. Friedl, J. Locker, E. Sahai, and J. E. Segall, Classifying collective cancer cell invasion, Nat. Cell Biol. **14**, 777 (2012).

[4] D. Weaire, F. Bolton, T. Herdtle, and H. Aref, The effect of strain upon the topology of a soap froth, Philos. Mag. Lett. **66**, 293 (1992).

[5] R. Etournay, M. Popović, M. Merkel, A. Nandi, C. Blasse, B. Aigouy, H. Brandl, G. Myers, G. Salbreux, F. Jülicher *et al.*, Interplay of cell dynamics and epithelial tension during morphogenesis of the *Drosophila* pupal wing, eLife **4**, e07090 (2015).

[6] B. Guirao, S. U. Rigaud, F. Bosveld, A. Bailles, J. López-Gay, S. Ishihara, K. Sugimura, F. Graner, and Y. Bellaïche, Unified quantitative characterization of epithelial tissue development, eLife **4**, e08519 (2015).

[7] K. D. Irvine and E. Wieschaus, Cell intercalation during *Drosophila* germband extension and its regulation by pair-rule segmentation genes, Development **120**, 827 (1994).

[8] R. Keller, L. Davidson, A. Edlund, T. Elul, M. Ezin, D. Shook, and P. Skoglund, Mechanisms of convergence and extension by cell intercalation, Philos. Trans. R. Soc. Lond. B **355**, 897 (2000).

[9] E. Walck-Shannon and J. Hardin, Cell intercalation from top to bottom, Nat. Rev. Mol. Cell Biol. **15**, 34 (2014).

[10] L. Oswald, S. Grosser, D. M. Smith, and J. A. Käs, Jamming transitions in cancer, J. Phys. D **50**, 483001 (2017).

[11] C. Bertet, L. Sulak, and T. Lecuit, Myosin-dependent junction remodelling controls planar cell intercalation and axis elongation, Nature (London) **429**, 667 (2004).

[12] M. Takeichi, Dynamic contacts: Rearranging adherens junctions to drive epithelial remodelling, Nat. Rev. Mol. Cell Biol. **15**, 397 (2014).

[13] M. Rauzi, Cell intercalation in a simple epithelium, Philos. Trans. R. Soc. B **375**, 20190552 (2020).

[14] M. Rauzi, P. Verant, T. Lecuit, and P.-F. Lenne, Nature and anisotropy of cortical forces orienting *Drosophila* tissue morphogenesis, Nat. Cell Biol. **10**, 1401 (2008).

[15] G. B. Blanchard, A. J. Kabla, N. L. Schultz, L. C. Butler, B. Sanson, N. Gorfinkiel, L. Mahadevan, and R. J. Adams, Tissue tectonics: Morphogenetic strain rates, cell shape change and intercalation, Nat. Methods **6**, 458 (2009).

[16] B. Aigouy, R. Farhadifar, D. B. Staple, A. Sagner, J.-C. Röper, F. Jülicher, and S. Eaton, Cell flow reorients the axis of planar polarity in the wing epithelium of Drosophila, Cell **142**, 773 (2010).

[17] S. Curran, C. Strandkvist, J. Bathmann, M. de Gennes, A. Kabla, G. Salbreux, and B. Baum, Myosin II controls junction fluctuations to guide epithelial tissue ordering, Dev. Cell **43**, 480 (2017).

[18] S. Kim, M. Pochitaloff, G. A. Stooke-Vaughan, and O. Campàs, Embryonic tissues as active foams, Nat. Phys. **17**, 859 (2021).

[19] H. P. Jain, A. Voigt, and L. Angheluta, Robust statistical properties of T1 transitions in a multi-phase field model of cell monolayers, Sci. Rep. **13**, 10096 (2023).

[20] D. Bi, J. H. Lopez, J. M. Schwarz, and M. L. Manning, A density-independent rigidity transition in biological tissues, Nat. Phys. **11**, 1074 (2015).

[21] D. L. Barton, S. Henkes, C. J. Weijer, and R. Sknepnek, Active vertex model for cell-resolution description of epithelial tissue mechanics, PLoS Comput. Biol. **13**, e1005569 (2017).

[22] R. Alert, J. Casademunt, and J.-F. Joanny, Active turbulence, Annu. Rev. Condens. Matter Phys. **13**, 143 (2022).

[23] A. Doostmohammadi, J. Ignés-Mullol, J. M. Yeomans, and F. Sagués, Active nematics, Nat. Commun. **9**, 3246 (2018).

[24] J.-M. Armengol-Collado, L. N. Carenza, J. Eckert, D. Krommydas, and L. Giomi, Epithelia are multiscale active liquid crystals, Nat. Phys. **19**, 1773 (2023).

[25] G. Duclos, C. Erlenkämper, J.-F. Joanny, and P. Silberzan, Topological defects in confined populations of spindle-shaped cells, Nat. Phys. **13**, 58 (2017).

[26] T. B. Saw, A. Doostmohammadi, V. Nier, L. Kocgozlu, S. Thampi, Y. Toyama, P. Marcq, C. T. Lim, J. M. Yeomans, and B. Ladoux, Topological defects in epithelia govern cell death and extrusion, Nature (London) **544**, 212 (2017).

[27] T. Lecuit and A. S. Yap, E-cadherin junctions as active mechanical integrators in tissue dynamics, Nat. Cell Biol. **17**, 533 (2015).

[28] D. Wenzel, M. Nestler, S. Reuther, M. Simon, and A. Voigt, Defects in active nematics—Algorithms for identification and tracking, Comput. Methods Appl. Math. **21**, 683 (2021).

[29] M. Nonomura, Study on multicellular systems using a phase field model, PLoS ONE **7**, e33501 (2012).

[30] B. A. Camley, Y. Zhang, Y. Zhao, B. Li, E. Ben-Jacob, H. Levine, and W. J. Rappel, Polarity mechanisms such as contact inhibition of locomotion regulate persistent rotational motion of mammalian cells on micropatterns, Proc. Natl. Acad. Sci. USA **111**, 14770 (2014).

[31] J. Löber, F. Ziebert, and I. S. Aranson, Collisions of deformable cells lead to collective migration, Sci. Rep. **5**, 1 (2015).

[32] B. Palmieri, Y. Bresler, D. Wirtz, and M. Grant, Multiple scale model for cell migration in monolayers: Elastic mismatch between cells enhances motility, Sci. Rep. **5**, 11745 (2015).

[33] W. Marth and A. Voigt, Collective migration under hydrodynamic interactions: A computational approach, Interface Focus **6**, 20160037 (2016).

[34] R. Mueller, J. M. Yeomans, and A. Doostmohammadi, Emergence of active nematic behavior in monolayers of isotropic cells, Phys. Rev. Lett. **122**, 048004 (2019).

[35] D. Wenzel and A. Voigt, Multiphase field models for collective cell migration, Phys. Rev. E **104**, 054410 (2021).

[36] M. Salvalaglio, A. Voigt, and S. M. Wise, Doubly degenerate diffuse interface models of surface diffusion, Math. Methods Appl. Sci. **44**, 5385 (2021).

[37] R. Gu, X. Wang, and M. Gunzburger, Simulating vesicle-substrate adhesion using two phase field functions, J. Comput. Phys. **275**, 626 (2014).

[38] H. P. Jain, D. Wenzel, and A. Voigt, Impact of contact inhibition on collective cell migration and proliferation, Phys. Rev. E **105**, 034402 (2022).

[39] L. Shen, P. Lin, Z. Xu, and S. Xu, Diffuse interface model for cell interaction and aggregation with Lennard-Jones type potential, Comput. Methods Appl. Mech. Eng. **415**, 116257 (2023).

[40] L. Happel and A. Voigt, Coordinated motion of epithelial layers on curved surfaces, Phys. Rev. Lett. **132**, 078401 (2024).

[41] S. Vey and A. Voigt, AMDiS: Adaptive multidimensional simulations, Comput. Vis. Sci. **10**, 57 (2007).

[42] T. Witkowski, S. Ling, S. Praetorius, and A. Voigt, Software concepts and numerical algorithms for a scalable adaptive parallel finite element method, Adv. Comput. Math. **41**, 1145 (2015).

[43] S. Praetorius and A. Voigt, *Collective Cell Behaviour—A Cell-Based Parallelisation Approach for a Phase Field Active Polar Gel Model*, NIC Series No. 49 (Forschungszentrum Jülich GmbH, Zentralbibliothek, Jülich, 2018).

[44] See Supplemental Material at http://link.aps.org/supplemental/10.1103/PhysRevResearch.6.033176 for Movie of simulation as per parameters in Table 1, and movies of evolution of $|\mathbf{p}^-_{T1}(\mathbf{x})|$, $|\mathbf{p}^+_{T1}(\mathbf{x})|$, $\bar{v}^-_{T1}(\mathbf{x})$ and $\bar{v}^+_{T1}(\mathbf{x})$.

[45] L. Giomi, J. Toner, and N. Sarkar, Hydrodynamic theory of p-atic liquid crystals, Phys. Rev. E **106**, 024701 (2022).

[46] L. Giomi, J. Toner, and N. Sarkar, Long-ranged order and flow alignment in sheared p-atic liquid crystals, Phys. Rev. Lett. **129**, 067801 (2022).

[47] J. P. Sethna, K. A. Dahmen, and C. R. Myers, Crackling noise, Nature (London) **410**, 242 (2001).